IEEE Access
Multidisciplinary | Rapid Review | Open Access Journal

Received April 1, 2020, accepted April 11, 2020, date of publication April 14, 2020, date of current version April 29, 2020.

Digital Object Identifier 10.1109/ACCESS.2020.2987872

Analysis of a Tooth-Coil Winding Permanent-Magnet Synchronous Machine With an Unequal Teeth Width

ALVARO E. HOFFER[1,2], (Student Member, IEEE), ILYA PETROV[2], JUHA J. PYRHÖNEN[2], (Senior Member, IEEE), JUAN A. TAPIA[1], (Senior Member, IEEE), AND GERD BRAMERDORFER[3], (Senior Member, IEEE)

[1]Department of Electrical Engineering, University of Concepción, Concepción 4070386, Chile
[2]Department of Electrical Engineering, LUT University, 53851 Lappeenranta, Finland
[3]Department of Electrical Drives and Power Electronics, Johannes Kepler University Linz, 4040 Linz, Austria

Corresponding author: Alvaro E. Hoffer (ahoffer@udec.cl)

This work was supported in part by the LUT University, Finland, and in part by the Comisión Nacional de Investigación Científica y Tecnológica (CONICYT), Chile through Project Fondecyt, under Grant 1171508.

ABSTRACT This paper presents an analysis of a permanent magnet synchronous machine (PMSM) with an unequal teeth width. The use of the concentrated nonoverlapping winding, also known as tooth-coil winding, has certain advantages. In addition, asymmetric features can be exploited by adopting this winding configuration to improve the machine performance. The procedure involves increasing the stator tooth width and, to the same extent, reducing the adjacent stator tooth width. In this paper, an analytical method was employed to predict and understand the back-EMF behavior, and a finite element analysis (FEA) was performed to verify the analytical method. Furthermore, a detailed study of the machine performance (electromagnetic torque, flux density, and losses) was carried out by the FEA. The machine was built and tested to validate the performance of the machine.

INDEX TERMS Analytical analysis, asymmetrical stator, finite element analysis, permanent magnet, permanent magnet machine, tooth-coil winding.

NOMENCLATURE

α	Mechanical position.
β	Electrical position.
Ω	Mechanical angular speed.
$2p$	Number of poles.
Q_s	Number of slots.
v, v_1, v_2	-th harmonic number.
q	Number of slots per pole and phase.
CT	Goodness factor (related to cogging torque).
GCD	Greatest common divisor.
LCM	Least common multiple.

I. INTRODUCTION

Permanent magnet synchronous machines provide certain advantages over other traditional machines because of their high torque/volume ratio, high power factor, and high efficiency [1], [2]. Depending on the type of winding, PMSMs exhibit different characteristics. The most commonly used winding types in PMSMs are nonoverlapping concentrated windings (CW) and distributed windings (DW) [3]. Distributed windings are characterized by producing a close to sinusoidal current linkage (or magnetomotive force) waveform yet avoiding significant current linkage low-order harmonic components because of the consequent distribution of the coils along the stator periphery ($q \geq 1$). In contrast, concentrated windings, also known as tooth-coil windings (TCW), have high contents of space harmonics (often including significant subharmonics) in the current linkage waveform, with a highly nonsinusoidal shape [4], [5]. However, the TCW presents various advantages such as a higher power density, excellent fault tolerance (the contact between conductors of different phases is reduced or even eliminated) and easier manufacture [3], [6]. Moreover, the amount of copper

The associate editor coordinating the review of this manuscript and approving it for publication was Su Yan.

used in the end winding is reduced because of its short length, which means a reduction in the winding Joule losses and the machine weight [7]. Therefore, the TCW has significant advantages, which makes it suitable for various applications, particularly in power generators, owing to the great benefits in electrical insulation [8].

Asymmetric features can be exploited by adopting the TCW configuration to improve the machine performance. In [9], it is shown that the back-EMF and the electromagnetic torque can be maximized by employing an unequal teeth width in nonoverlapping CW permanent magnet (PM) brushless machines. According to [9], by increasing the width of the stator teeth that carry a coil, the flux linkage can be maximized. The maximum value of flux linkage is achieved when the coil pitch is equal to the pole pitch. In addition, it is possible to reduce the torque ripple. However, the analysis is limited to machines with small tooth-tips or closed slots.

A novel technique to minimize the torque ripple in a rotor surface PMSM and interior PMSM was investigated in [10]. In the paper, it was stated that the unbalanced flux density of the teeth results in some high-order harmonics of the torque ripple. It was proposed that these harmonics can be minimized by employing an unequal teeth width. However, the method is limited to a single operating point. In [11], it was reported that TCW PMSMs have a strong magnetic saturation as a result of the interaction of the armature and PM reaction fluxes, which has a significant impact on the torque quality and leads to a nonsymmetric flux distribution. Asymmetries in the rotor pole (slit implementation) and asymmetries in the stator teeth were investigated in order to decrease the local magnetic saturation and enhance the torque characteristics.

A new asymmetrical rotor hybrid CW PMSM with enhanced torque performance was presented in [12]. It was proposed to modify the rotor structure of a conventional symmetrical rotor hybrid spoke-type PM motor by asymmetric positioning of the upper part of the PMs to improve torque production. The main idea of the study was to adjust the reluctance torque component to reach the maximum value at the same current phase angle at which the excitation torque is at the maximum. The machine was investigated by the finite element analysis (FEA), achieving satisfactory results.

In [13], a 12-slot 10-pole PMSM 4-layer winding having coils with different numbers of turns was introduced. The total number of conductors per slot was kept constant to have an invariant slot space factor. Asymmetry allows improving the air gap flux density waveform, canceling lowest-order subharmonics, which could lead to an improvement in the machine performance.

In [14], a modular machine with an unequal teeth width was proposed. A machine of this kind employs CW, and it consists of independent modules with single-layer winding. It was found that flux gaps (air gaps between modules) and an unequal teeth width improve the air gap flux density. Furthermore, the applied flux gaps between the segments can improve the winding similarly to machines with an unequal teeth width, as mentioned in [9]. However, the machine performance can be degraded or improved according to the slot/pole number combination by applying different flux gap widths.

Numerous studies on the asymmetries in TCW PMSMs suggest that there is a wide range of options to enhance the machine performance. Furthermore, the asymmetries not only aim to improve typical motor characteristics (such as torque/power or back-EMF), but they can, for instance, minimize the pulsating torque. However, to the authors' knowledge, only a few studies have been reported in which the effect of asymmetries has been analyzed by analytical methods. This is possibly due to the complexity of the machine geometry that applies an asymmetric structure, which complicates analytical approaches. However, under certain assumptions, it is possible to predict and understand the actual phenomena with analytical methods. Nevertheless, the FEA is essential in the study, as it considers the effects that are neglected in the simplified analytical analysis.

This article proposes a comprehensive study about the influence of the unequal teeth width on the air gap flux density, the flux linkage, the back-EMF, the electromagnetic torque, and the losses of the TCW PMSM. A different approach to calculate the back-EMF in a TCW PMSM with an unequal teeth width is presented. The proposed method makes use of existing methods found in the literature such as in [15]. The existing methods are focused on symmetric machines. However, the proposed method takes into account the effect of the unequal teeth width. Furthermore, the proposed method incorporates the influence of the slotting effect and the skewing, in contrast with the investigated in [9]. Finally, with the use of the proposed method it was possible to discover in detail the base phenomena, which affected the performance variation of the studied machine when going to asymmetric stator structure. This helps in understanding the extra optimization rules applied to TCW PMSM that can further improve specific characteristics of the designed machines.

The paper is organized as follows: First, the topology of the proposed asymmetry is delineated along with its advantages, and some characteristics to be taken into account to achieve a better machine performance are presented. Next, the machine under study is described. Then, the permeance distribution of the machine is analyzed. The proposed method to obtain the complex permeance distribution is verified by the FEA. After that, the back-EMF is studied using the modified analytical method and the FEA. The explanation of the variation in the back-EMF when using an unequal teeth width is based on the analytical results. An accurate study of the machine performance (electromagnetic torque, flux density, and losses) is carried out by the FEA. Finally, the machine is built, and an experimental test is carried out to validate the performance of the machine.

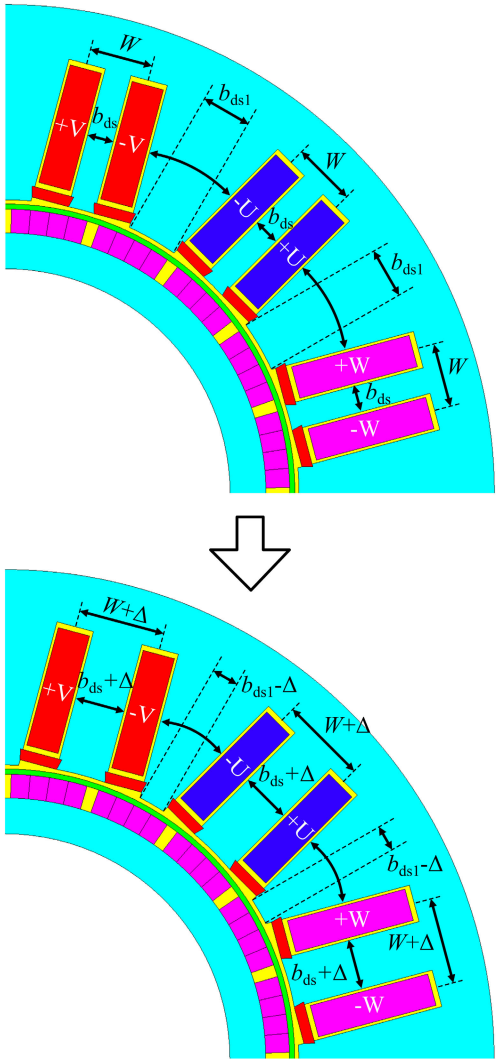

FIGURE 1. Adjustment of the stator inner tooth width b_{ds}. The stator slot width b_s is kept constant.

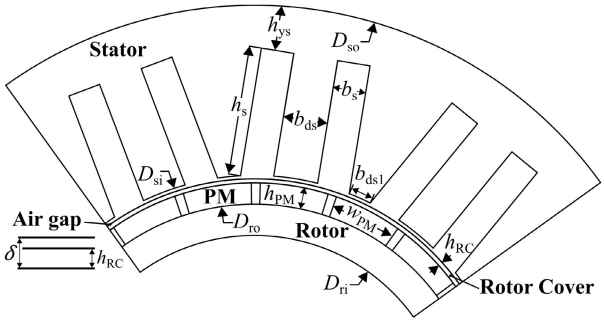

FIGURE 2. Geometric structure of the PMSM under study.

TABLE 1. Parameters of the PMSM.

Parameter	Value
Rated power P_N (W)	1700
Rated torque T_N (Nm)	202
Rated frequency f_N (Hz)	13.33
Rated stator current I_{sN} (Arms)	9.4
Rated mechanical speed n_N (rpm)	80
Number of stator slots Q_s	24
Number of poles $2p$	20
Stator outer diameter D_{so} (mm)	369.9
Stator inner diameter D_{si} (mm)	222.1
Stator yoke depth h_{ys} (mm)	19.9
Stator slot width b_s (mm)	14.25
Stator inner tooth width[1] b_{ds} (mm)	19.0
Stator inner tooth width[2] b_{ds1} (mm)	10.27
Physical air gap length δ (mm)	3.5
Rotor outer diameter D_{ro} (mm)	197.1
Rotor inner diameter D_{ri} (mm)	170.0
Rotor cover thickness h_{RC} (mm)	2.0
Permanent magnet width w_{PM} (mm)	27.9
Permanent magnet height h_{PM} (mm)	9.0
Number of turns per phase N_{ph}	232
Stator winding resistance R_{ph} (Ω)	1.1
Synchronous inductance L_s (H)	0.027
Winding connection	star

[1]Tooth that carries a coil
[2]Tooth that does not carry a coil
*Symmetric stator: $b_{ds} = b_{ds1} = 14.65$ mm

II. TCW PMSM WITH AN UNEQUAL TEETH WIDTH

A. FEATURES OF TCW PMSM WITH AN UNEQUAL TEETH WIDTH

The aim of using an unequal teeth width is to increase the flux linkage and thus, enhance the torque capability and the back-EMF. The procedure involves increasing the stator tooth width and, to the same extent, reducing the adjacent stator tooth width, as shown in Fig. 1. Because of the nonuniform stator teeth, it is possible to use only a single-layer (SL) winding. The advantage of employing the SL winding is that the distribution factor is the maximum possible for that number of slots per pole and phase, which means that the winding factor is higher compared with a greater number of winding layers if a three-phase system is applied [16]. According to Fig. 1, the coil pitch W depends on the stator inner tooth width b_{ds} and the stator slot width b_s (which is kept constant). Therefore, the performance of the machine is evaluated based on the width of the tooth that carries a coil.

Previous studies have investigated feasible pole/slot number combinations for the TCW with $q \leq 0.5$ [4]. In addition, the pole/slot combination should satisfy $GCD(Q_s, p) > 1$ to avoid unbalanced magnetic pull [3], and $CT = 2\,pQ_s/LCM(Q_s, 2\,p)$ must be low enough in order to achieve a low inherent cogging torque [17]. Other features to be considered are the mutual coupling factor and the air gap harmonic leakage factor. The factors must be small or negligible to ensure a fault-tolerant machine with magnetically decoupled phases and a high performance [5].

B. MACHINE DESCRIPTION

The machine under study is a radial flux PMSM, which is designed to be submersible in water. The machine can operate for instance as a pump motor or a generator for tidal energy harvesting. The machine geometry is presented in Fig. 2. The parameters and geometric dimensions of the submersible PMSM design are listed in Table 1. The geometric parameters

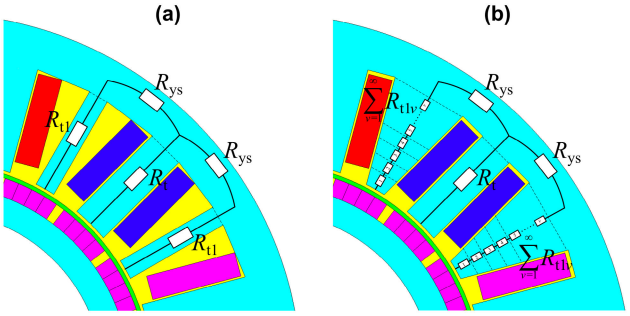

FIGURE 3. Stator slot geometry and teeth reluctances: (a) trapezoidal slot and (b) rectangular slot. The trapezoidal teeth reluctance (b) is smaller than the rectangular teeth reluctance (a).

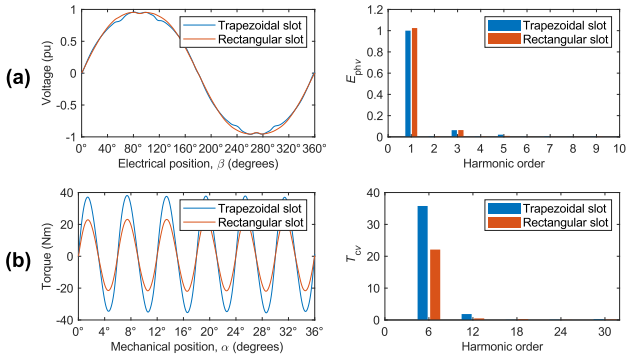

FIGURE 4. (a) Phase back-EMF and (b) cogging torque when using trapezoidal and rectangular slots. FEA.

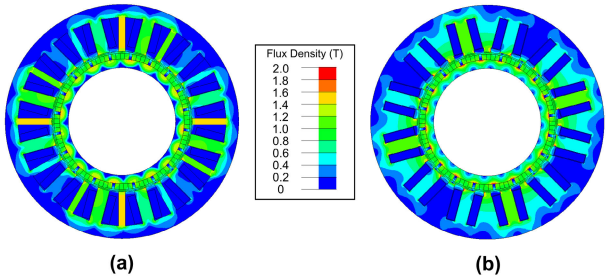

FIGURE 5. Flux density distribution under no-load when using (a) trapezoidal slot and (b) rectangular slot. FEA.

are chosen based on the magnetic and the electric loading of the machine. The value of the stator inner tooth width b_{ds} is chosen to increase the back-EMF over the symmetric machine without changing the external dimensions of the machine and, keeping the machine losses at fair value. However, it is beyond the scope of this paper.

The structure comprises an inner rotor and an outer stator. The PMs are mounted on the rotor surface, because such a construction can be used with a rotor yoke made of a simple solid core tube. PMs have a curved shape to align the PM surface with the rotor core surface. In order to reduce the eddy-current losses in the PMs, each magnet block is separated into four segments. The rotor is protected from the water environment by a cover, as the PMs are vulnerable to corrosion.

The PM material used in the construction is N45SH Neodymium Magnet with the remanent flux density of 1.36 T at 20 °C, the relative permeability of 1.05, and the isotropic resistivity of 180×10^{-8} Ω ·m at 20 °C. The rotor core is made of construction steel S355 (also known as Fe52) as it exhibits acceptable magnetic and mechanical properties. Moreover, it has a relatively high electrical resistivity to reduce the eddy-current losses in the rotor as a result of the current linkage of the low-order harmonics when the TCW with a single-layer approach is used [18]. The material selected for the rotor cover is glass fibre composite (GFC), because it has a high electrical resistivity and it is nonmagnetic.

The stator is not protected by any cover because the selected active materials in the stator are resistant to corrosion. The stator core is made of 430 stainless steel grade (430SS). The 430SS is a ferritic stainless steel that has excellent corrosion resistance and good magnetic properties (compared with other stainless steel materials), along with acceptable market availability. The isotropic resistivity of 430SS is 60×10^{-8} Ω ·m at room temperature. Polyvinyl chloride (PVC) insulated wires with solid conductors are selected as the winding material, because they provide high-quality insulation and are entirely water-resistant.

The stator contains a three-phase winding held in place in rectangular slots. The rectangular slot was chosen in comparison with the trapezoidal slot because it improves the machine performance and enables easier manufacture and assembly of the prewound coils. Fig. 3 shows the rectangular and trapezoidal slots and the equivalent magnetic reluctance in the stator core. When the stator slot is rectangular, the magnetic reluctance of the trapezoidal tooth is smaller than the magnetic reluctance of the rectangular tooth. Therefore, the magnetic flux is slightly increased when using rectangular slots, which indicates an increase in the back-EMF, as shown in Fig. 4(a). Moreover, the cogging torque is reduced by 40%, as it can be seen in Fig. 4(b). The decrease in the magnetic saturation in the stator teeth explains the reduction in the cogging torque, as seen in Fig. 5. Despite the improvements in the rectangular slot, the peak-to-peak value of the cogging torque still reaches 18% of the rated torque, which supports the use of skewing for further cogging torque reduction. The highest cogging torque harmonic component of the nonskewed machine is of the sixth order. Hence, to eliminate this particular harmonic, a two-step rotor skewing with a shift of 30 electrical degrees (3 mechanical degrees) between the magnet layers is applied.

III. THE PERMEANCE DISTRIBUTION IN THE AIR GAP

The permeance distribution in the air gap of a TCW PMSM with an unequal teeth width can be calculated to investigate the behavior of the back-EMF and the electromagnetic torque by varying the coil-carrying stator tooth width. The approach to obtain the permeance distribution in the air gap for a

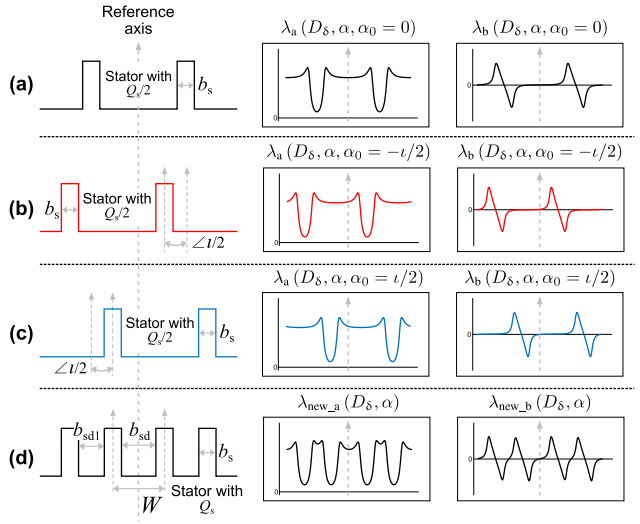

FIGURE 6. Sequence of the estimation of the permeance distribution in the air gap of a TCW PMSM with an unequal teeth width. The angle $\iota = 360°/(Q_s/2) - W$ corresponds to the angular displacement between two neighboring slots that carry different phase coils.

symmetric stator is described in [15]. The model is constructed by using a Schwarz-Christoffel transformation. The assumptions applied in this method are the following: (i) the permeability of iron is infinite, (ii) the stator slots have an infinite depth, and (iii) the height of the core is infinite.

The complex relative permeance distribution in the air gap of a machine with a number of slots Q_s can be expressed in the form of a Fourier series as

$$\lambda_a(D_\delta, \alpha, \alpha_0) = \sum_{v=0}^{N_\lambda} \lambda_{av}(D_\delta) \cos(vQ_s(\alpha - \alpha_0)) \quad (1)$$

$$\lambda_b(D_\delta, \alpha, \alpha_0) = \sum_{v=1}^{N_\lambda} \lambda_{bv}(D_\delta) \sin(vQ_s(\alpha - \alpha_0)), \quad (2)$$

where D_δ is the air gap diameter, α_0 is the reference angle, N_λ is the maximum order of the Fourier coefficients, and λ_{av} and λ_{bv} are the real and imaginary parts of the Fourier coefficients of the permeance function in the air gap with an equal teeth width representing the amplitudes of the permeance harmonics in the air gap. The coefficients are calculated from the air gap permeance waveforms as described in [15] using a discrete Fourier transform.

Sequence of the estimation of the permeance distribution in the air gap of a TCW PMSM with an unequal teeth width is shown in Fig. 6. Diagram to obtain the permeance distribution in the air gap of a TCW PMSM with an unequal teeth width is depicted in Fig. 7. The algorithm to obtain the new permeance distribution is arranged as follows:

1) First, obtain the permeance distribution waveforms for a symmetric stator with half of the slots ($Q_s/2$) shown in Fig. 6(a) according to [15].

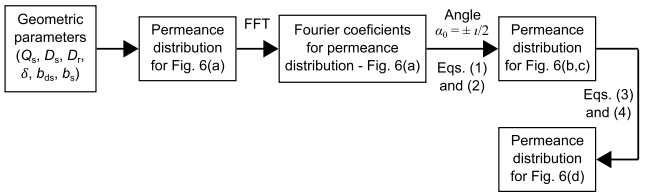

FIGURE 7. Diagram to obtain the permeance distribution in the air gap of a TCW PMSM with an unequal teeth width.

2) Calculate the Fourier coefficients of the permeance distribution in the air gap (λ_{av} and λ_{bv}) obtained for the case Fig. 6(a).
3) With the calculated coefficients, obtain the complex permeance distribution waveforms with reference angles equal to $\alpha_0 = -\iota/2$ and $\alpha_0 = \iota/2$, which refer to slot positions of Fig. 6(b) and (c), respectively. The new permeance distribution waveforms have an offset from the initial symmetric stator, specified by the new reference angle that coincides with the axis of the tooth that carries a coil around itself. In this way, the asymmetrical position of adjacent slots can be considered.
4) Combining the Fourier coefficients of the waveforms derived from Fig. 6(b, c), it is possible to find the overall real and imaginary components of the new permeance distribution in the air gap of the machine under study, which can be expressed as

$$\lambda_{new\_a}(D_\delta, \alpha) = \lambda_a(D_\delta, \alpha, \alpha_0 = -\iota/2) \times \lambda_a(D_\delta, \alpha, \alpha_0 = \iota/2) \quad (3)$$

$$\lambda_{new\_b}(D_\delta, \alpha) = \lambda_b(D_\delta, \alpha, \alpha_0 = -\iota/2) + \lambda_b(D_\delta, \alpha, \alpha_0 = \iota/2). \quad (4)$$

Equation (3) corresponds to the multiplication of the real components of the permeance distributions derived from Fig. 6(b, c), which are shifted by ι from each other and (4) corresponds to the sum of the imaginary components of the same permeance distributions.
5) Calculate new Fourier coefficients (λ_{new_av} and λ_{new_bv}) from the results obtained in the previous step using a discrete Fourier transform. The waveforms can be expressed in the form of a Fourier series as

$$\lambda_{new\_a}(D_\delta, \alpha) = \sum_{v=0}^{N_\lambda} \lambda_{new\_av}(D_\delta) \cos\left(v\frac{Q_s}{4}\alpha\right) \quad (5)$$

$$\lambda_{new\_b}(D_\delta, \alpha) = \sum_{v=1}^{N_\lambda} \lambda_{new\_bv}(D_\delta) \cos\left(v\frac{Q_s}{4}\alpha\right), \quad (6)$$

where the 1/4 factor that multiplies the number of slots results from the new waveform period that considers the asymmetry (unequal teeth width and two stator slots).

The permeance distributions in the air gap calculated by the analytical model and the FEA for $b_{ds} = b_{ds1}$ (symmetric

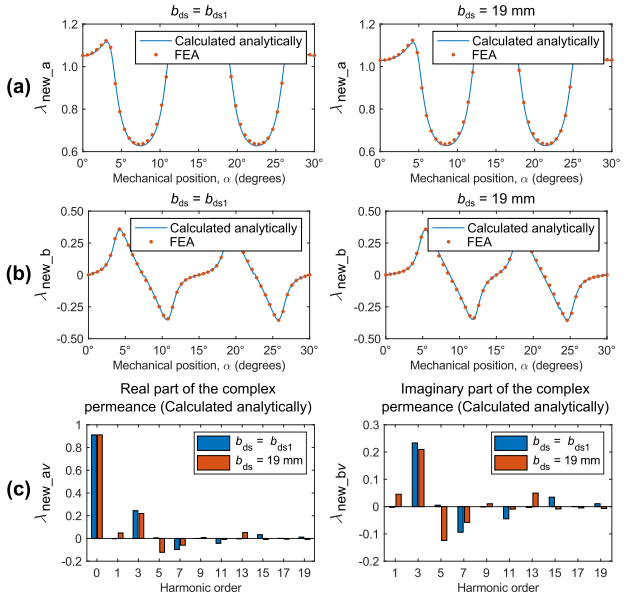

FIGURE 8. **Complex permeance distribution in the air gap of the symmetric stator $b_{ds} = b_{ds1}$ and the asymmetric stator with $b_{ds} = 19$ mm: (a) real part, (b) imaginary part, and (c) spectra.**

stator) and the asymmetric stator (having $b_{ds} = 19$ mm) are shown in Fig. 8(a) and Fig. 8(b), respectively. There is a good agreement between both the analytical models and the FEA results. The results show that the proposed method allows obtaining the permeance distribution in the air gap of TCW PMSMs with an unequal teeth width. It is pointed out that adjusting the value of b_{ds} changes the spectrum of permeances in which new harmonics appear or the value of existing harmonics are modified, as shown in Fig. 8(c). It influences the machine performance, as it will be shown in the next sections.

The proposed method to obtain the permeance distribution of a TCW PMSM with an unequal teeth width can be used to calculate the back-EMF, the cogging torque, the electromagnetic torque, and related variables using the appropriate analytical models available in the literature [9], [19]–[21].

IV. BACK-EMF CALCULATION

The normal component of the flux density distribution in the slotted air gap induced only by PMs is given by

$$B_{\mathrm{n}}(D_\delta, \alpha, t) = B_{\mathrm{n\_sl}}(D_\delta, \alpha, t)\,\lambda_{\mathrm{new\_a}}(D_\delta, \alpha) + B_{\mathrm{tan\_sl}}(D_\delta, \alpha, t)\,\lambda_{\mathrm{new\_b}}(D_\delta, \alpha), \quad (7)$$

where $B_{\mathrm{n\_sl}}$ and $B_{\mathrm{tan\_sl}}$ are the radial and tangential components of the flux density in the slotless air gap induced only by PMs, calculated according to [15], respectively.

The flux linkage in the phase winding can be calculated as

$$\begin{aligned}\psi_{\mathrm{ph}}(t) &= N_{\mathrm{ph}} l' \frac{D_\delta}{2} \int_{-\frac{W}{2}}^{\frac{W}{2}} B_{\mathrm{n}}(D_\delta, \alpha, t)\,\mathrm{d}\alpha \\ &= \sum_{v_1=1,3,5,\ldots}^{\infty} N_{\mathrm{ph}} l' \frac{D_\delta}{2} k_{\mathrm{sq}v_1} k_{\mathrm{so}v_1} \left\{ 2\lambda_{\mathrm{new\_a0}} B_{\mathrm{n\_sl}v_1} \frac{k_{\mathrm{p}v_1}}{v_1 p} \right. \\ &\quad + \sum_{v_2=1}^{N_\lambda} \begin{pmatrix} B_{\mathrm{n\_sl}v_1}\lambda_{\mathrm{new\_a}v_2} \\ -B_{\mathrm{t\_sl}v_1}\lambda_{\mathrm{new\_b}v_2} \end{pmatrix} \cdot \frac{\sin\left[\left(v_1 p + v_2 \frac{Q_{\mathrm{s}}}{4}\right)\frac{W}{2}\right]}{v_1 p + v_2 \frac{Q_{\mathrm{s}}}{4}} \\ &\quad \left. + \sum_{v_2=1}^{N_\lambda} \begin{pmatrix} B_{\mathrm{n\_sl}v_1}\lambda_{\mathrm{new\_a}v_2} \\ +B_{\mathrm{t\_sl}v_1}\lambda_{\mathrm{new\_b}v_2} \end{pmatrix} \cdot \frac{\sin\left[\left(v_1 p - v_2 \frac{Q_{\mathrm{s}}}{4}\right)\frac{W}{2}\right]}{v_1 p - v_2 \frac{Q_{\mathrm{s}}}{4}} \right\} \\ &\quad \cdot \cos(v_1 p \Omega t), \end{aligned} \quad (8)$$

where $\lambda_{\mathrm{new\_a0}}$ is the average of the complex permeance distribution, N_{ph} is the number of turns per phase, l' is the stator stack length, $k_{\mathrm{p}v}$ is the pitch factor, $k_{\mathrm{sq}v}$ is the skewing factor, and $k_{\mathrm{so}v}$ is the slot opening factor. The factor expressions are described in Appendix A.

The back-EMF can be calculated from the derivative of the flux linkage per pole as

$$\begin{aligned} e_{\mathrm{ph}}(t) &= -\frac{\mathrm{d}\psi_{\mathrm{ph}}(t)}{\mathrm{d}t} \\ &= \sum_{v_1=1,3,5,\ldots}^{\infty} N_{\mathrm{ph}} l' \frac{D_\delta}{2} k_{\mathrm{sq}v_1} k_{\mathrm{so}v_1} \Omega \left\{ 2\lambda_{\mathrm{new\_a0}} B_{\mathrm{n\_sl}v_1} k_{\mathrm{p}v_1} \right. \\ &\quad + \sum_{v_2=1}^{N_\lambda} \begin{pmatrix} B_{\mathrm{n\_sl}v_1}\lambda_{\mathrm{new\_a}v_2} \\ -B_{\mathrm{t\_sl}v_1}\lambda_{\mathrm{new\_b}v_2} \end{pmatrix} \cdot \frac{\sin\left[\left(v_1 p + v_2 \frac{Q_{\mathrm{s}}}{4}\right)\frac{W}{2}\right]}{v_1 p + v_2 \frac{Q_{\mathrm{s}}}{4}} \\ &\quad \left. + \sum_{v_2=1}^{N_\lambda} \begin{pmatrix} B_{\mathrm{n\_sl}v_1}\lambda_{\mathrm{new\_a}v_2} \\ +B_{\mathrm{t\_sl}v_1}\lambda_{\mathrm{new\_b}v_2} \end{pmatrix} \cdot \frac{\sin\left[\left(v_1 p - v_2 \frac{Q_{\mathrm{s}}}{4}\right)\frac{W}{2}\right]}{v_1 p - v_2 \frac{Q_{\mathrm{s}}}{4}} \right\} \\ &\quad \cdot \sin(v_1 p \Omega t), \end{aligned} \quad (9)$$

Equation (8) can be divided into two parts. The first term corresponds to the base magnetic flux and the second term to an additional magnetic flux caused by the interaction between the permeance distribution and the air gap flux density—the sum of both magnetic flux components results in the main magnetic flux. When the stator slots are closed, the imaginary part of the complex permeance is neglected. As a result, the normal component of the air gap flux density depends only on the flux density induced by the PMs, and the flux linkage per pole can be optimized based on the pitch factor. When the stator slots are open, the average magnetic flux is reduced because of the slotting effect. Despite this, it is possible to enhance the flux linkage per pole owing to the base magnetic flux and the additional magnetic flux.

Fig. 9 shows the waveforms of the air gap flux density for different stator inner tooth widths b_{ds} (tooth containing the coil). By increasing the value of b_{ds}, the integration area of the magnetic flux increases, including a greater amount of magnetic flux. However, when the coil pitch is greater than the pole pitch, the base magnetic flux is reduced because of the opposite flux of the adjacent PM. Nevertheless, the additional magnetic flux could mitigate the opposite flux, translating the maximum value of the magnetic flux by a single tooth

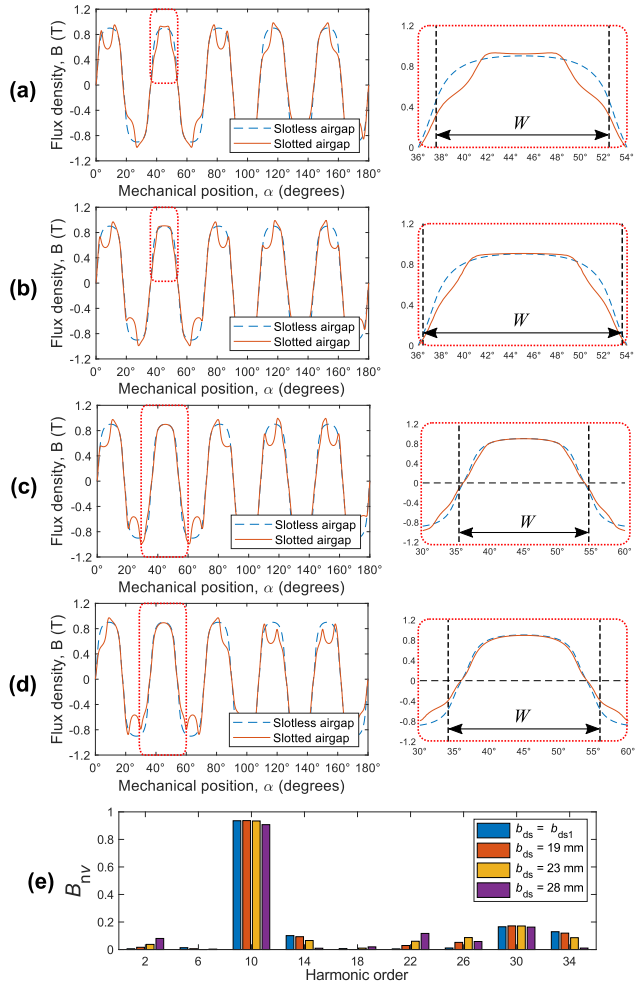

FIGURE 9. No-load air gap flux density waveform over the base machine with a scaled air gap flux density distribution over the stator tooth containing the coil at different tooth widths: (a) $b_{ds} = b_{ds1}$, (b) $b_{ds} = 19$ mm, (c) $b_{ds} = 23$ mm, (d) $b_{ds} = 28$ mm, and (e) spectra. Calculated analytically.

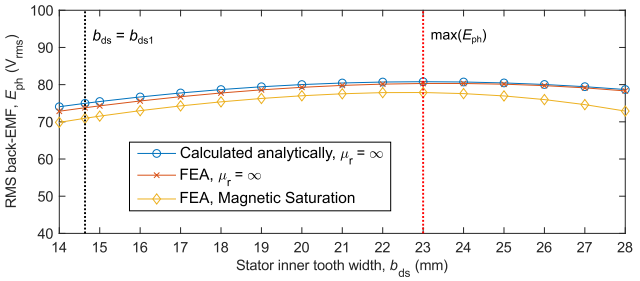

FIGURE 10. RMS back-EMF value at the nominal speed calculated by analytical and FEA models as a function of stator inner tooth width b_{ds}.

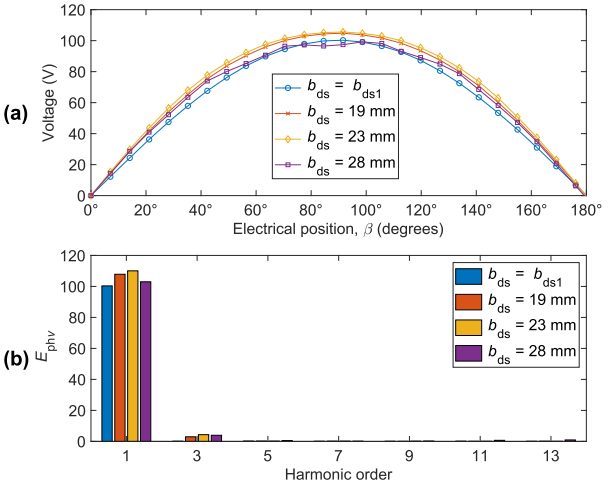

FIGURE 11. (a) Back-EMF waveforms at the nominal speed for different stator inner tooth widths b_{ds} values and (b) their spectra. FEA.

predicted by the pitch factor ($W = \tau_p = 34$ mm $\Rightarrow b_{ds} = 20$ mm).

Based on the above discussion, it is possible to enhance the flux linkage per phase and the back-EMF by adjusting the stator inner tooth width b_{ds}. The minimum and maximum values of b_{ds} depend on the stator inner diameter, the stator slot width, and the number of slots. However, it is necessary to verify the performance of the machine for each case individually.

The RMS back-EMF value as a function of the stator inner tooth width b_{ds} at the rated speed is depicted in Fig. 10. Based on the results, there is a good agreement between the analytical model and the FEA when the core permeability is assumed infinite. When the magnetic saturation is considered, the RMS back-EMF decays faster once it reaches the maximum value ($b_{ds} = 23$ mm). It can be explained by the nonlinear behavior of the magnetic core material. The back-EMF can be adjusted at a higher value with respect to the symmetric stator ($b_{ds} = b_{ds1}$). For $b_{ds} = 19$ mm, the back-EMF increases approximately by 8% with respect to the symmetric stator.

The back-EMF waveforms for different values of the stator inner tooth width b_{ds} at the rated speed computed by the FEA are shown in Fig. 11. It should be noted that the waveforms are symmetrical, even though the arrangement of the slots is asymmetric. This could be explained by the use of the theory of the star of slots [22]. The star of slots for the combination of 24 slots and 20 poles for the symmetric machine is shown in Fig. 12(a). In this case, the angle between the phasors of two adjacent slots is the mechanical angle α_s (the electrical angle is denoted by $\alpha_s^e = p \cdot \alpha_s$), and it coincides with the coil pitch W as a result of the pole/slot number combination. However, when choosing a value of b_{ds} greater than the original value, the angle between the phasors of the same coil α_{s1} is different from the angle between the phasors of different coils α_{s2}. Nevertheless, the sum of the α_{s1} and α_{s2} angles is constant and corresponds to $360°/(Q_s/2)$, which is equivalent to the angular displacement of two stator slot widths and the unequal teeth width. The resulting star of slots for a value of b_{ds} greater than the original value is shown in Fig. 12(b). The back-EMF of each coil is represented by a phasor in the star of slots. The resulting three-phase back-EMF phasor diagrams for $b_{ds} = b_{ds1}$ and $b_{ds} > b_{ds1}$ are depicted in Fig. 12(c) and Fig. 12(d), respec-

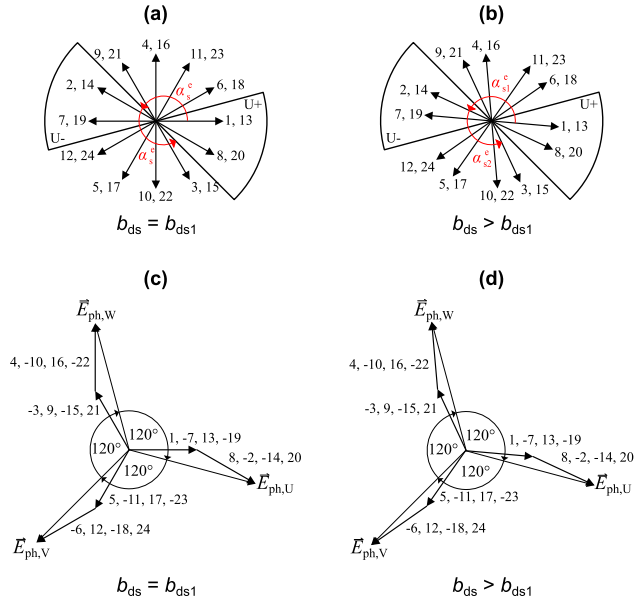

FIGURE 12. Star of slots of a three-phase 24-slot 20-pole machine for (a) $b_{ds} = b_{ds1}$ and (b) $b_{ds} > b_{ds1}$. The resulting three-phase back-EMF phasor diagram for (c) $b_{ds} = b_{ds1}$ and (d) $b_{ds} > b_{ds1}$.

tively, where the angles between the phases are 120 electrical degrees. It can be seen that the angle between the phasors of the different phases remains invariant in both cases, which explains the symmetric back-EMF induced waveforms.

V. TORQUE ANALYSIS

The influence of the unequal teeth width on the electromagnetic torque (EM) of the machine under study is investigated. In order to compare the electromagnetic torque for the nonskewed and the two-step skewed rotor, stator current maps were computed by the FEA as a function of the stator inner tooth width b_{ds} and electromagnetic torque T_{em} as shown in Fig. 13. The machine was driven with an $i_d = 0$ control. Based on the results, with the nonskewed machine, it is possible to achieve higher values of electromagnetic torque than with the skewed machine when applying the same supply current. In both cases, by increasing the value of b_{ds} for the same stator current, the electromagnetic torque increases slightly until $b_{ds} = 23$ mm and then begins to decrease because of the lower magnetic flux. Thereafter, it is necessary to increase the stator current to reach similar torque values. Thus, it is not advisable to choose values higher than 23 mm for b_{ds}, as it could reduce the torque capability and the machine efficiency.

The cogging torque and the torque ripple for the nonskewed and two-step skewing machines were evaluated as a function of the stator inner tooth width b_{ds} as shown in Fig. 14. In addition, the electromagnetic torque variation for the symmetric stator ($b_{ds} = b_{ds1}$) and $b_{ds} = 19$ mm at the rated current is shown in Fig. 15. The results in Fig. 14 indicate that the primary source of torque ripple is the cogging torque. For the nonskewed machine, the high peak-to-peak

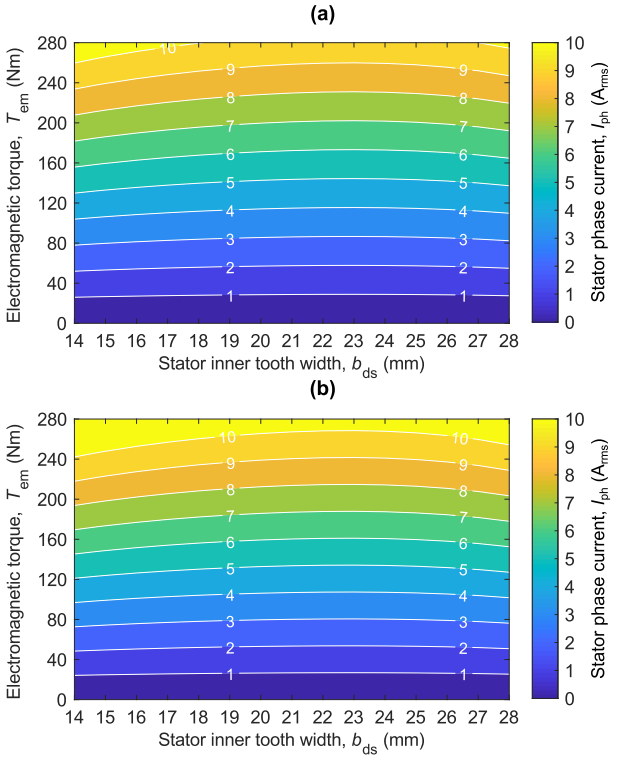

FIGURE 13. Stator current maps for (a) nonskewed rotor and (b) two-step skewed rotor. FEA.

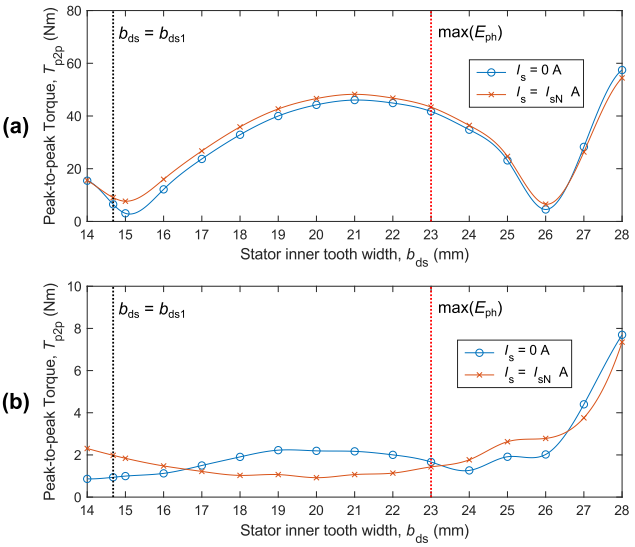

FIGURE 14. Cogging torque and torque ripple as a function of the stator inner tooth width b_{ds} for: (a) nonskewed rotor and (b) two-step skewed rotor. FEA.

values of the pulsating torque are explained by the asymmetric stator structure, which makes it necessary to consider the application of skew. The geometrical periodicity of the asymmetric stator core is half that of the symmetrical stator core. When two-step skewing is applied, the 6th harmonic is reduced, as shown in Fig. 15. However, the higher order torque ripple harmonics (e.g. 12th) are not eliminated. Therefore, to eliminate higher order harmonics, it is necessary

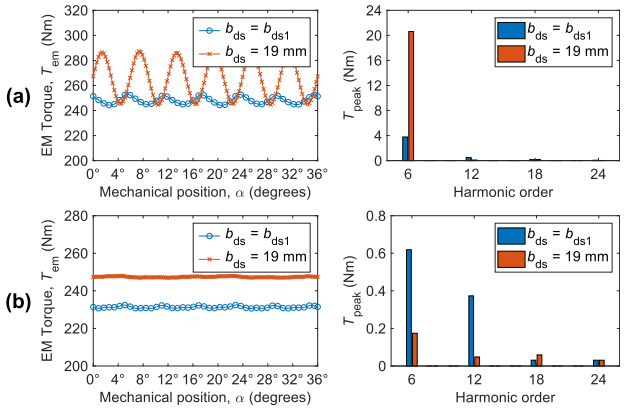

FIGURE 15. Electromagnetic torque variation over one electrical period: (a) nonskewed rotor and (b) two-step skewed rotor. FEA.

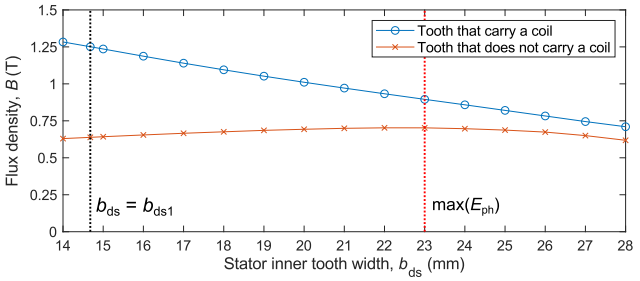

FIGURE 16. Maximum flux density of the stator teeth as a function of the stator inner tooth width b_{ds}. FEA.

to apply more skewing steps (which would make the rotor assembly more difficult) or another skew angle, which would not eliminate the strongest harmonic component (6^{th}).

VI. ANALYSIS OF THE FLUX DENSITY AND MUTUAL COUPLING BETWEEN PHASES

Fig. 16 shows the maximum flux density of the tooth that carries a coil and a tooth that does not carry a coil as a function of the stator inner tooth width b_{ds} when the machine operates at the rated current and speed. It is pointed out that the flux density values in the tooth that does not carry a coil are lower than the flux density values in the tooth that carries a coil. This is explained by the fact that the magnetic flux flows through the tooth that carries a coil, after which it divides, passing a part of the magnetic flux in the tooth that does not carry a coil. It means that with an unequal teeth width in a machine it is possible to achieve a better performance than with a symmetric machine because of the lower magnetic saturation. However, it is necessary to verify the flux density variation of the stator teeth over one electrical period. Fig. 17 shows the waveforms of the flux density of the teeth and their harmonic spectra for the symmetric stator ($b_{ds} = b_{ds1}$) and $b_{ds} = 19$ mm. Furthermore, their flux density distributions are shown in Fig. 18. The results show that the harmonic content is low for both cases. The presence of high harmonic content can be a restriction when choosing the value of b_{ds}.

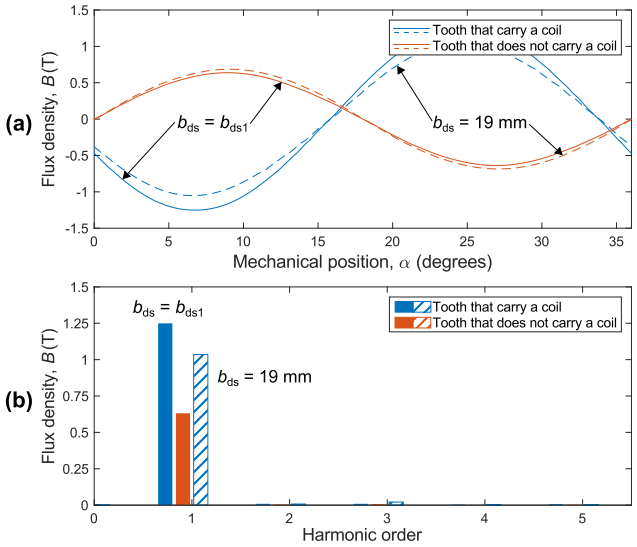

FIGURE 17. (a) Flux density variation of the stator teeth over one electrical period and (b) their spectra. FEA.

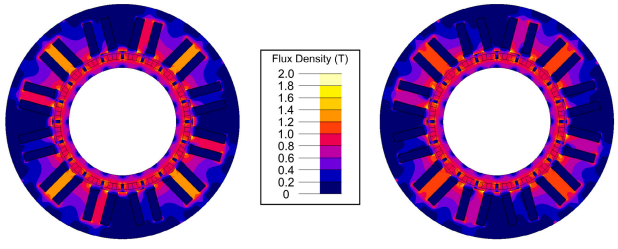

FIGURE 18. Flux density distribution under load for (a) symmetric stator ($b_{ds} = b_{ds1}$) and (b) asymmetric stator with $b_{ds} = 19$ mm. FEA.

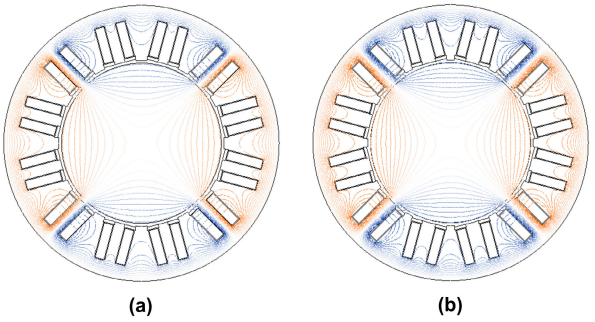

FIGURE 19. Flux plot when only phase U is supplied for (a) symmetric stator ($b_{ds} = b_{ds1}$) and (b) asymmetric stator with $b_{ds} = 19$ mm. FEA.

The mutual coupling between phases was verified for the symmetric stator ($b_{ds} = b_{ds1}$) and $b_{ds} = 19$ mm. Because of the slot/pole combination chosen, the mutual coupling factor is zero [5], [22]. Fig. 19 shows the magnetic flux lines when only phase U is supplied. Note that the magnetic flux is linked only by the coils carrying current. Therefore, it is found that the asymmetry does not affect the fault tolerance of the machine.

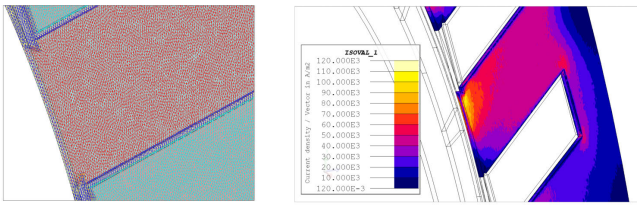

(a) (b)

FIGURE 20. (a) Mesh quality and (b) current density distribution of the stator core. FEA.

TABLE 2. PMSM losses at the rated point. FEA.

Parameter	$b_{ds} = b_{ds1}$	$b_{ds} = 19$ mm
Winding Joule losses (W)	333.50	291.60
Stator eddy current losses (W)	3.5	3.5
Rotor eddy current losses (W)	12.82	16.83
PM Joule losses (W)	0.61	0.61

VII. MACHINE LOSSES

In order to analyze the machine performance, the losses were calculated. The winding Joule losses are determined by [23],

$$P_{Cu} = Q_s z_Q^2 \rho_{Cu} \left(\frac{l' + l_w}{S_{slot} k_{Cu}} \right) I_s^2, \tag{10}$$

where z_Q is the number of conductors in one slot, ρ_{Cu} is the copper resistivity, k_{Cu} is the copper space factor, l' is the stator stack length, l_W is the end-winding length, and I_s is the RMS stator current. The end-winding length depends on the stator inner tooth width b_{ds}. However, because of the machine size, the stator resistance is considered constant for the cases discussed here.

The PM Joule losses, the rotor eddy current losses, and the stator eddy current losses were computed by the FEA. In particular, the stator eddy current losses were calculated by the 3D FEA model (core sheet) with a fine mesh (see Fig. 20(a) to obtain accurate results. Fig. 20(b) shows the current density distribution in a single stator sheet at the rated current. A comparison of the losses for the symmetric stator ($b_{ds} = b_{ds1}$) and $b_{ds} = 19$ mm at the rated point is shown in Table 2.

According to the preliminary results, the highest losses of the machine are caused by the winding Joule losses. Moreover, the PM losses are low for both cases because of the low electrical conductivity of the PM material and the PM segmentation. The stator eddy-current losses are low because of the good electrical properties of the magnetic material, very low rotational speed, and the low harmonic content of the flux density in the core.

The rotor Joule losses are higher than the stator Joule losses because the rotor core is a solid tube. Moreover, by increasing the stator inner tooth width b_{ds}, the rotor losses are increased. It can be explained by the increase in the amplitude of the current linkage subharmonics, as presented in Fig. 21. According to [18], the rotor losses in a TCW PMSM are mainly due to the low-order current linkage harmonics (subharmonics).

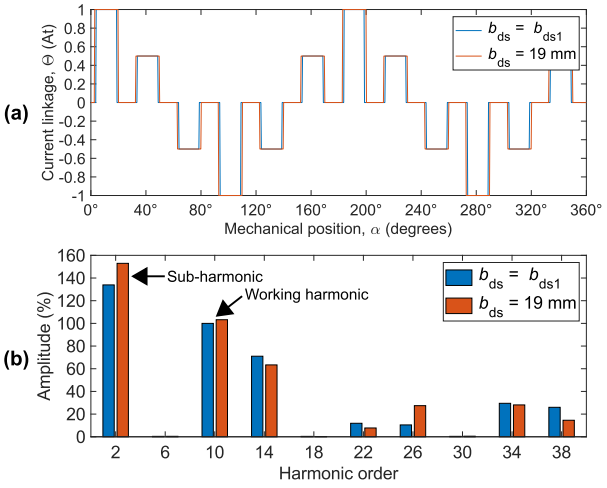

FIGURE 21. (a) Current linkage waveforms and (b) their spectra for the symmetric stator ($b_{ds} = b_{ds1}$) and the asymmetric stator with $b_{ds} = 19$ mm. Current linkage harmonic contents are normalized with respect to the working harmonic of the symmetric stator. Calculated analytically.

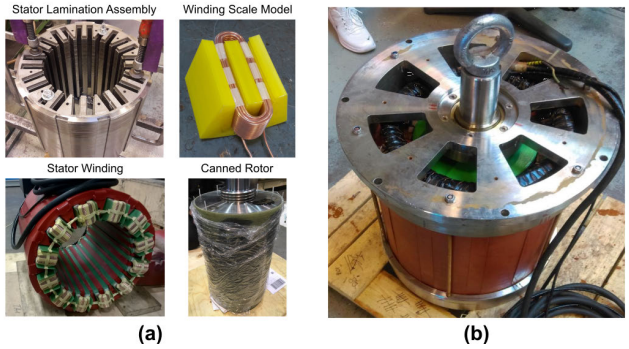

FIGURE 22. (a) Prototype machine parts and (b) prototype machine assembly.

Based on the results, it can deduced that when using an unequal teeth width in a TCW PMSM, it is possible to reach the same torque value at a lower stator current. Moreover, the winding Joule losses are reduced resulting in improved efficiency.

VIII. EXPERIMENTAL VALIDATION

A prototype machine was built to verify the predictions. The different machine parts are shown in Fig. 22(a), and the machine assembly in Fig. 22(b).

The prototype was validated by an experimental test carried out in a test bench as shown in Fig. 23(a). A schematic view of the experimental setup is depicted in Fig. 23(b). The prototype is coupled to an induction machine (IM), where the IM operates as a dynamometer. The prototype was immersed in a container with water at ambient temperature according to the operating specifications of the machine. The measurement of torque and speed was performed with a Magtrol torque transducer coupled to the shaft. The voltage and current measurements in the prototype were carried out with a Yokogawa PZ4000 Power Analyzer. The data were

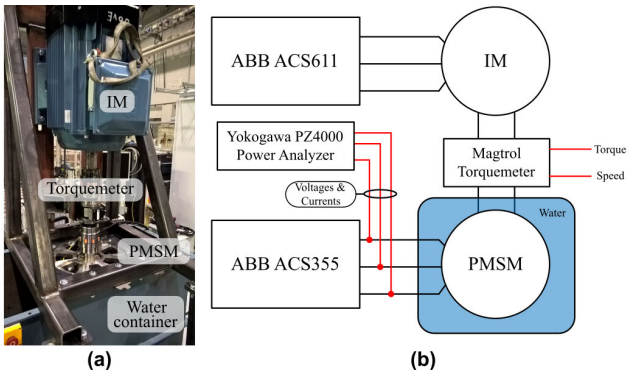

FIGURE 23. (a) Prototype machine in the test bench and (b) connection scheme for the experimental setup (instruments, converters, IM dynamometer, and prototype machine).

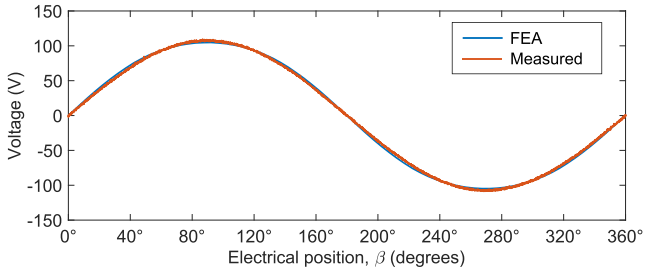

FIGURE 24. Simulated and measured back-EMF waveforms at the rated speed.

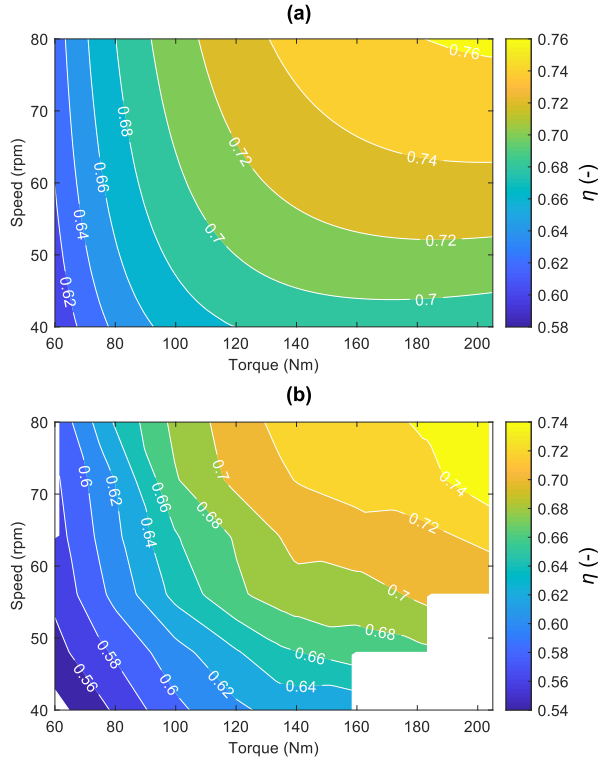

FIGURE 25. (a) Estimated (FEA) and (b) measured efficiency maps.

acquired and processed. Measurements at different levels of load and speed were performed.

A comparison between the back-EMF obtained by the FEA and measured at the rated speed is shown in Fig. 24. The error between the FEA result and the experimental test is 4% (peak-to-peak voltage).

A constant detent torque was measured at different speeds when measuring the back-EMF. The value obtained was approximately 30 Nm at any speed. The detent torque corresponds to the sum of the stator core hysteresis and friction losses. The detent torque corresponds to 20% of the rated torque of the machine, which means that it must be analyzed further. According to the preliminary analysis results, this detent torque is mostly caused by relatively high hysteresis losses in the stainless steel applied in the stator core. However, the study of the detent torque is beyond the scope of this paper.

The estimated and measured efficiency maps are shown in Fig. 25. The detent torque was included in the FEA model for efficiency estimation to make a more fair comparison of the efficiency maps. Based on the results, there is a similar behavior between the efficiency maps. The maximum efficiency of 74% is reached at the rated point. The low efficiency is explained by the winding Joule losses, the detent torque, and the very low rotational speed.

IX. CONCLUSION

In this paper, an analysis of a TCW PMSM with an unequal teeth width was presented. The stator asymmetry was used to optimize the machine performance. This was achieved by varying the value of the stator tooth width. The mean value of the electromagnetic torque was improved. Thus, it is possible to obtain similar torques by adjusting the stator tooth width while applying lower current values, resulting in a reduction in the winding Joule losses. The obtained back-EMF waveform is symmetrical, and the mutual coupling phase remains invariant. Thus, the asymmetries in the stator can be used without a significant effect on other machine characteristics. The overall flux density in the stator teeth was reduced by using asymmetric teeth width. However, owing to the concentrated winding type with a single layer, the rotor losses were increased. The next step (which is out of the scope of this paper) is an in-depth analysis of the hysteresis losses in the stator core when adjusting the value of the stator inner tooth width, which might have a significant effect on the machine efficiency.

APPENDIX A
FACTOR EXPRESSIONS

The pitch factor is expressed as [24]

$$k_{pv} = \sin\left(v\frac{\pi}{2}\frac{W}{\tau_p}\right), \tag{11}$$

where v is the harmonic order, $W = b_{ds} + b_s$ is the coil pitch, which depends on the stator inner tooth width b_{ds} and the stator slot width b_s, and $\tau_p = \pi D_\delta / 2p$ is the pole pitch, which depends on the air gap diameter and the number of poles $2p$.

The slot opening factor can be calculated as [25]

$$k_{sov} = \frac{\sin\left(v\frac{\pi}{2}\frac{b_0}{\tau_p}\right)}{\left(v\frac{\pi}{2}\frac{b_0}{\tau_p}\right)}, \tag{12}$$

where b_0 is the slot opening, which in this work coincides with the stator slot width b_s. The skewing factor is obtained as [24], [26]

$$k_{sqv} = \frac{\sin\left(vp\frac{\gamma}{2}\right)}{\left(vp\frac{\gamma}{2}\right)}, \tag{13}$$

where p is the number of pole pairs and γ is the continuous skewing angle (mechanical angle).

The use of these factors is necessary for the analytical calculation of the flux linkage per pole and the back-EMF. Not considering the factor expressions results in inaccurate calculation of the back-EMF waveform (and related variables) and its harmonics components.

ACKNOWLEDGMENT

The authors would like to thank Dr. has been. Niemelä, LUT University, Finland, for her linguistic assistance in the preparation of this manuscript.

REFERENCES

[1] Y.-P. Yang and M.-T. Peng, "A surface-mounted permanent-magnet motor with sinusoidal Pulsewidth-Modulation-Shaped magnets," *IEEE Trans. Magn.*, vol. 55, no. 1, pp. 1–8, Jan. 2019.
[2] M. J. Melfi, S. Evon, and R. McElveen, "Induction versus permanent magnet motors: For power density and energy savings in industrial applications," *IEEE Ind. Appl. Mag.*, vol. 15, no. 6, pp. 28–35, 2009.
[3] D. Martínez, "Design of a permanent-magnet synchronous machine with non-overlapping concentrated windings for the shell eco marathon urban prototype," M.S. thesis, KTH, Elect. Energy Convers., Stockholm, Sweden, 2012.
[4] P. Ponomarev, P. Lindh, and J. Pyrhonen, "Effect of slot-and-pole combination on the leakage inductance and the performance of tooth-coil permanent-magnet synchronous machines," *IEEE Trans. Ind. Electron.*, vol. 60, no. 10, pp. 4310–4317, Oct. 2013.
[5] P. Ponomarev, Y. Alexandrova, I. Petrov, P. Lindh, E. Lomonova, and J. Pyrhonen, "Inductance calculation of tooth-coil permanent-magnet synchronous machines," *IEEE Trans. Ind. Electron.*, vol. 61, no. 11, pp. 5966–5973, Nov. 2014.
[6] N. Bianchi, S. Bolognani, and M. D. Pre, "Magnetic loading of fractional-slot three phase PM motors with non-overlapped coils," in *Proc. Conf. Rec. IEEE Ind. Appl. Conf., 41st IAS Annu. Meeting*, vol. 1, Oct. 2006, pp. 35–43.
[7] A. M. EL-Refaie, "Fractional-slot concentrated-windings synchronous permanent magnet machines: Opportunities and challenges," *IEEE Trans. Ind. Electron.*, vol. 57, no. 1, pp. 107–121, Jan. 2010.
[8] J. Zhao, Y. Liu, and X. Xu, "Comparisons of concentrated and distributed winding PMSM in MV power generation," in *Proc. 12th Int. Conf. Electr. Mach. (ICEM)*, Sep. 2018, pp. 2437–2443.
[9] D. Ishak, Z. Q. Zhu, and D. Howe, "Permanent-magnet brushless machines with unequal tooth widths and similar slot and pole numbers," *IEEE Trans. Ind. Appl.*, vol. 41, no. 2, pp. 584–590, Mar. 2005.
[10] I. Petrov, P. Ponomarev, Y. Alexandrova, and J. Pyrhonen, "Unequal teeth widths for torque ripple reduction in permanent magnet synchronous machines with fractional-slot non-overlapping windings," *IEEE Trans. Magn.*, vol. 51, no. 2, pp. 1–9, Feb. 2015.
[11] I. Petrov, P. Ponomarev, and J. Pyrhönen, "Asymmetrical geometries in electrical machines," *Int. Rev. Electr. Eng. (IREE)*, vol. 11, no. 1, p. 20, 2016.
[12] X. Zeng, L. Quan, X. Zhu, L. Xu, and F. Liu, "Investigation of an asymmetrical rotor hybrid permanent magnet motor for approaching maximum output torque," *IEEE Trans. Appl. Supercond.*, vol. 29, no. 2, pp. 1–4, Mar. 2019.
[13] A. Tessarolo, M. Mezzarobba, and N. Barbini, "Improved four-layer winding design for a 12-slot 10-pole permanent magnet machine using unequal tooth coils," in *Proc. 42nd Annu. Conf. IEEE Ind. Electron. Soc. (IECON)*, Oct. 2016, pp. 1686–1691.
[14] G. J. Li and Z. Q. Zhu, "Analytical modeling of modular and unequal tooth width surface-mounted permanent magnet machines," *IEEE Trans. Magn.*, vol. 51, no. 9, pp. 1–9, Sep. 2015.
[15] D. Zarko, D. Ban, and T. A. Lipo, "Analytical calculation of magnetic field distribution in the slotted air gap of a surface permanent-magnet motor using complex relative air-gap permeance," *IEEE Trans. Magn.*, vol. 42, no. 7, pp. 1828–1837, Jul. 2006.
[16] L. Alberti and N. Bianchi, "Theory and design of fractional-slot multilayer windings," *IEEE Trans. Ind. Appl.*, vol. 49, no. 2, pp. 841–849, Mar. 2013.
[17] Z. Q. Zhu and D. Howe, "Influence of design parameters on cogging torque in permanent magnet machines," *IEEE Trans. Energy Convers.*, vol. 15, no. 4, pp. 407–412, 2000.
[18] N. Bianchi, S. Bolognani, and E. Fornasiero, "An overview of rotor losses determination in three-phase fractional-slot PM machines," *IEEE Trans. Ind. Appl.*, vol. 46, no. 6, pp. 2338–2345, Nov. 2010.
[19] D. Zarko, D. Ban, and T. A. Lipo, "Analytical solution for cogging torque in surface permanent-magnet motors using conformal mapping," *IEEE Trans. Magn.*, vol. 44, no. 1, pp. 52–65, Jan. 2008.
[20] D. Zarko, D. Ban, and T. A. Lipo, "Analytical solution for electromagnetic torque in surface permanent-magnet motors using conformal mapping," *IEEE Trans. Magn.*, vol. 45, no. 7, pp. 2943–2954, Jul. 2009.
[21] A. Rahideh, M. Mardaneh, and T. Korakianitis, "Analytical 2-D calculations of torque, inductance, and back-EMF for brushless slotless machines with surface inset magnets," *IEEE Trans. Magn.*, vol. 49, no. 8, pp. 4873–4884, Aug. 2013.
[22] N. Bianchi and M. Dai Pre, "Use of the star of slots in designing fractional-slot single-layer synchronous motors," *IEE Proc.-Electr. Power Appl.*, vol. 153, no. 3, pp. 459–466, 2006.
[23] G.-J. Li, Z.-Q. Zhu, M. P. Foster, D. A. Stone, and H.-L. Zhan, "Modular permanent-magnet machines with alternate teeth having tooth tips," *IEEE Trans. Ind. Electron.*, vol. 62, no. 10, pp. 6120–6130, Oct. 2015.
[24] J. Pyrhönen, T. Jokinen, and V. Hrabovcovó, *Design of Rotating Electrical Machines*. Hoboken, NJ, USA: Wiley, 2013.
[25] S. G. Min and B. Sarlioglu, "Analytical calculation of back EMF waveform for linear PM motors in slotted and slotless structures," *IEEE Trans. Magn.*, vol. 53, no. 12, pp. 1–10, Dec. 2017.
[26] N. Bianchi and S. Bolognani, "Design techniques for reducing the cogging torque in surface-mounted PM motors," *IEEE Trans. Ind. Appl.*, vol. 38, no. 5, pp. 1259–1265, Sep. 2002.

ALVARO E. HOFFER (Student Member, IEEE) was born in Temuco, Chile, in 1991. He received the B.Eng. and M.Eng. degrees in electrical engineering from the Universidad de la Frontera, Temuco, in 2016. He is currently pursuing the Ph.D. degree with the Department of Electrical Engineering, University of Concepción, Chile, and the Department of Electrical Engineering, LUT University, Finland, through a double degree (DD) agreement. His current research interests include the field of electrical machines and drives, and renewable energies.

ILYA PETROV received the D.Sc. degree from the Lappeenranta University of Technology (LUT), Finland, in 2015. He is currently a Researcher with the Department of Electrical Engineering, LUT.

JUHA J. PYRHÖNEN (Senior Member, IEEE) was born in Kuusankoski, Finland, in 1957. He received the D.Sc. degree from the Lappeenranta University of Technology (LUT), Finland, in 1991. He became an Associate Professor of electrical engineering at LUT, in 1993, and a Professor of electrical machines and drives, in 1997. He is engaged in research and development of electric motors and electric drives. His current research interests include different synchronous machines and drives, induction motors and drives, and solid-rotor high-speed induction machines and drives.

JUAN A. TAPIA (Senior Member, IEEE) received the B.Sc. and M.Sc. degrees in electrical engineering from the University of Concepción, Concepción, Chile, in 1991 and 1997, respectively, and the Ph.D. degree from the University of Wisconsin, WI, Madison, in 2002. From 2010 to 2014, he was a FiDiPro Fellow with the Academy of Finland, Lappeenranta University of Technology, Lappeenranta, Finland, where he conducted research on PM machines with LUT energy. He is currently working as an Associate Professor with the Department of Electrical Engineering, University of Concepción. His research interests include electrical machine design, numerical methods for electromagnetic fields, DSP-based electric machine control, and renewable energy.

GERD BRAMERDORFER (Senior Member, IEEE) received the Ph.D. degree in electrical engineering from Johannes Kepler University Linz, Linz, Austria, in 2014.

He is currently an Assistant Professor with the Department of Electrical Drives and Power Electronics, Johannes Kepler University Linz. His current research interests include the design, modeling, and optimization of electric machines as well as magnetic bearings and bearingless machines.

Dr. Bramerdorfer is a Senior Member of the IEEE Industrial Electronics Society, the IEEE Industry Applications Society, and the IEEE Magnetics Society. He continuously serves the scientific community, e.g., as a Guest Editor, the Track Chair, and the Topic Chair, by organizing special sessions, and as a reviewer for journals and conferences. He is an Associate Editor of the IEEE Transaction on Industrial Electronics and an Editor of the IEEE Transactions on Energy Conversion.